Available online at www.sciencedirect.com
ScienceDirect
Acta Materialia 56 (2008) 2191–2202
Acta MATERIALIA
www.elsevier.com/locate/actamat

Strong violet–blue light photoluminescence emission at room temperature in $SrZrO_3$: Joint experimental and theoretical study

V.M. Longo [a,b], L.S. Cavalcante [a,b], R. Erlo [a,b], V.R. Mastelaro [c], A.T. de Figueiredo [a,b], J.R. Sambrano [d], S. de Lázaro [a,b], A.Z. Freitas [e], L. Gomes [e], N.D. Vieira Jr. [e], J.A. Varela [f], Elson Longo [f,*]

[a] *LIEC, Departamento de Ciências e Engenharia de Materiais, UFSCar, 13565-905, São Carlos, SP, Brazil*
[b] *LIEC, Departamento de Química, UFSCar, 13565-905, São Carlos, SP, Brazil*
[c] *Instituto de Física de São Carlos, USP, 13560-970 São Carlos, SP, Brazil*
[d] *Laboratorio de Simulação Molecular, DM, UNESP 17033-360, Bauru, SP, Brazil*
[e] *Center for Lasers and Applications, IPEN/CNEN-SP, Cidade Universitária, 05508-000 São Paulo, SP, Brazil*
[f] *LIEC, Instituto de Química, UNESP, 14801-970 Araraquara, SP, Brazil*

Received 24 August 2007; received in revised form 20 December 2007; accepted 20 December 2007
Available online 4 March 2008

Abstract

Ultrafine ordered and disordered $SrZrO_3$ powders were prepared by the polymeric precursor method. The structural evolution from structural disorder to order was monitored by X-ray diffraction and X-ray absorption near-edge spectroscopy. Complex cluster vacancies $[ZrO_5 \cdot V_O^Z]$ and $[SrO_{11} \cdot V_O^Z]$ (where $V_O^Z = V_O^X$, $V_O^{\cdot}$ and $V_O^{\cdot\cdot}$) were proposed for disordered powders. The intense violet–blue light photoluminescence emission measured at room temperature in the disordered powders was attributed to complex cluster vacancies. High-level quantum mechanical calculations within the density functional theory framework were used to interpret the experimental results.

Keywords: Density functional theory; Perovskites; Optical materials; Extended X-ray absorption fine structure; Order–disorder phenomena

1. Introduction

Ceramics with perovskite structures have been the subject of extensive research thanks to their important physical characteristics, chemical stability and mechanical properties [1]. Strontium zirconate, $SrZrO_3$ (SZ), is particularly interesting because of its high-temperature electronic properties. Recently perfected techniques have yielded large, highly perfect single crystals of SZ, which can be used as laser-host and substrate materials. In addition, SZ is suitable for use in high-temperature applications such as fuel cells, steam electrolysis and hydrogen gas sensors [2–4]. These properties are obtained when the oxide is doped with acceptor ions that exhibit protonic conduction at high temperature [5].

At room temperature, SZ has an orthorhombic phase, which was revealed by structural studies performed back in the 1950s and 1960s [6,7]. More recent studies [8–10] at high temperatures have shown that SZ undergoes three structural phase transitions, which are summarized as follows: first, orthorhombic (*Pbnm*) to orthorhombic (*Cmcm*) at 697 °C, then to tetragonal ($I4/mcm$) at 827 °C, and finally to cubic ($Pm\bar{3}m$) at 1127 °C.

The development of advanced semiconductor materials with wide band-gaps (2.0–5.0 eV) may give rise to new optoelectronic devices, particularly materials for application in the development of blue light-emitting diodes (LEDs) or visible-light lasers. In many optoelectronic devices, disordered insulators can replace single-crystal semiconductors, particularly when cost is an important factor [11].

* Corresponding author.
E-mail address: elson@iq.unesp.br (E. Longo).

1359-6454/$34.00
doi:10.1016/j.actamat.2007.12.059

We found that a series of structurally disordered perovskites (ABO_3, where A = Ca, Sr and Ba, and B = Ti and Zr), synthesized by a soft chemical process called the polymeric precursor method (PPM), show intense photoluminescence (PL) at room temperature when excited by a 488 nm laser excitation line [12–14]. We have reported several interesting properties of these ordered–disordered materials, including the fact that X-ray absorption near-edge spectroscopy (XANES) of the ST disordered powders [15] indicated the coexistence of two types of environments for titanium, namely fivefold [TiO_5] square-based pyramid and sixfold coordination [TiO_6] octahedron. The order was related to the presence of [TiO_6] clusters, whereas the disorder was related to the presence of [TiO_5] clusters. Ab initio calculations showed that localized levels above the valence band (VB) and below the conduction band (CB) appear in theoretical disordered models, and a charge transfer occurs from the [TiO_5] cluster to the [TiO_6] one. These additional levels explain the wide PL emission observed in disordered materials [13–16].

PL is a powerful tool for investigating the energy levels of materials. It is also one of the most effective tools for providing important information about the physical properties of materials at the molecular level, including shallow and deep level defects and gap-states [17].

Several reports in the literature explain the conditions that favor PL emission in materials presenting a degree of order–disorder [18–20]. The authors attribute the radiative decay process to distorted octahedral [18], self-trapped excitons, oxygen vacancies, surface states [19] and charge transfer via intrinsic defects inside an oxygen octahedron [20]. As can be seen, there is no general consensus in the literature about why and how radiative decay takes place in perovskite-like structures with a certain degree of disorder.

Intense violet PL emission has been reported in SZ nanocrystals and attributed to the existence of defect levels [21]. Recently, we reported the very strong violet–blue light luminescence behavior of SZ when excited by a 350.7 nm line of a krypton ion laser, as well as a model (the wide-band model) that discusses the conditions that favor the generation of intense PL emission before the excitation process [22].

In this work, experimental XANES and extended X-ray absorption spectroscopy (EXAFS) results were used to accurately monitor the structural changes of former (Zr) and modifier (Sr) lattices during the transformation of structures from the disordered to the ordered state. A theoretical approach was used to simulated these structural changes, which were observed in experimental results simulating three types of disorder in the crystalline (ordered) orthorhombic unit cell, as follows: in the network former (Zr), in the network modifier (Sr), and in the network former–modifier (Zr/Sr). Our aim with these models was not to represent the exact reality of the disordered structures but to offer a simple scheme enabling us to understand the effects of structural deformation on the electronic structure without completely suppressing the geometry of the cell, which is useful for periodic calculations.

A number of complementary experimental characterization techniques were used, such as optical-absorption and PL spectroscopy at two different wavelengths, to investigate the shallow and deep defects generated in the gap-state of disordered and ordered powders. Theoretical analysis of the projected density of states (DOS) and band structures (BAND) allowed us to demonstrate how different structural defects contribute to the disordered system and give rise to specific states in the forbidden gap. Thus, a synergetic strategy was applied to the experimental and electronic study to obtain a clearer physical picture of the luminescence behavior of the SZ perovskite structure.

2. Experimental

SZ powders were chemically prepared by the PPM [23]. Strontium nitrate ($Sr(NO_3)_2$) and zirconium *n*-propoxide ($Zr[O(C_3H_7)]_4$), both of 99.9% purity (Aldrich), ethylene glycol ($C_2H_6O_2$) of 99.0% purity (J.T. Baker), and citric acid ($C_6H_8O_7$) of 99.5% purity (Mallinckrodt) were used as raw materials. Zirconium citrate was formed by dissolving $Zr[O(C_3H_7)]_4$ in an aqueous solution of citric acid, in a molar ratio of 1 mol of Zr to 3 mol of citric acid, under constant stirring at 90 °C. The resulting solution was clear and homogeneous. $Sr(NO_3)_2$ was added to the zirconium citrate in a stoichiometric quantity of 1 mol of Sr to 1 mol Zr citrate solution. Ammonium hydroxide (NH_4OH; 30% in NH_3 (Synth)), was used to adjust the pH (pH 7–8) of the solution and to prevent precipitation of strontium citrate, which is favored in an acid solution. After homogenization of the solution containing Sr^{2+} cations, ethylene glycol was added to polymerize the citrate through a polyesterification reaction. The mass ratio of citric acid to ethylene glycol was fixed at 60:40. The solution was polymerized at 120 °C for 3 h, followed by thermal treatment at 350 °C for 4 h, which caused it to pulverize into powder. The precursor powder was then heat-treated in a tube furnace at temperatures of 425, 450, 475, 500, 525, 550, 575, 600 and 1250 °C for 2 h, at a heating rate of 1 °C min^{-1} in an oxygen atmosphere.

The SZ powders were structurally characterized by X-ray diffraction (XRD). The diffraction patterns were recorded on a Bragg–Brentano diffractometer (Rigaku-PCMax-2000) with Cu-Kα in a θ–2θ configuration, using a graphite monochromator. Two kinds of powders should be distinguished for a better understanding of this work: the first, structurally disordered, which was heat-treated below the crystallization temperature, and the second, structurally ordered, which reached crystallization. The spectral dependence of the optical absorbance of the ordered and disordered powders was measured at room temperature in the diffuse reflection mode, using a Cary 5G (Bruker) spectrophotometer. The PL spectra were collected with a Thermal Jarrel-Ash Monospec 27 monochromator and a Hamamatsu R446 photomultiplier. The PL spectra were collected with a digital monochromator internally integrated to a CCD with an optical resolution of

1 nm and an accuracy of 0.1 nm (Newport, OSM-400UV/VIS-U), using a time integration of 4 s (2.9×10^{-17} W per count/s) coupled to an optical fiber. The 355 nm excitation wavelength of a third harmonic of a Nd:YAG Q-switched laser (Brilliant B from Quantel) with a pulse duration of 4 ns and a repetition rate of 10 Hz was used, with an average energy of 4 mJ per pulse. The 460 nm excitation wavelength of a tunable optical parametric oscillator (OPO) pumped by 355 nm (3 W) of a Q-switched Nd:YAG laser was also used, with an average energy of 4 mJ per pulse. In both cases, the laser line was filtered out by a high-pass glass filter, i.e. LP 385 when exciting at 355 nm and LP 475 for laser excitation at 460 nm to avoid signal saturation of the CCD.

EXAFS spectra were collected only at the Zr K-edge, while XANES spectra were collected at the Sr and Zr K-edges. The EXAFS and XANES spectra were measured using a Si (220) monochromator in the D04B-XAFS1 beam line at the Brazilian Synchrotron Light Laboratory (LNLS). The samples were deposited on a polymeric membrane and the incident and transmitted X-ray beam were detected by ionization chambers filled with argon gas. The XANES spectra at both edges were measured from 50 eV below and 200 eV above the edge, with an energy step of 1.0 eV near the edge region. For purposes of comparison of different samples, all the XANES spectra were background removed and normalized, using as unity 100 eV after the edge. During the measurement, to provide good energy reproducibility during the XANES data collection, the energy calibration of the monochromator was checked during the collection of the sample data using Sr and Zr metal foils, respectively. The energy range of the Zr K-edge EXAFS spectra was 17,900–18,900 eV for the Zr K edge and was calibrated using Zr foil. Data were collected at room temperature using energy steps of 2 eV and an integration time of 3 s. Three EXAFS spectra were collected for each sample and the average spectrum was used analyze the data.

The EXAFS spectra were analyzed qualitatively using the program set written by Michalowicz [24] according to the procedures recommended and described by the International Workshop on Standards and Criteria in XAFS [25]. Due to the low signal-to-noise ratio at high K values, the analysis of the EXAFS spectra was limited to the maximum value of 11 Å^{-1}. After atomic absorption removal and normalization, the $k\chi(k)$ weighted EXAFS signal was Fourier transformed to R distance space in the 2.68–10.24 Å^{-1} k range. Each spectrum was Fourier transformed using a Kaiser apodization window with $\tau = 2.5$.

Over the past decade, improvements in computational methods and increasing computational power have attracted many research groups to address condensed system problems from first-principles calculations.

SZ crystallizes in an orthorhombic unit cell according to ICDD card 42–423 (*Pbnm*). The unit cell has 20 atoms containing four units of $SrZrO_3$. There are four nonequivalent atoms in the unit cell, with internal experimental values of Zr (0, 0, 0), Sr (0.00903, 0.46185, 0.25000), O1 (−0.07134, −0.02263, 0.25000) and O2 (0.20867, 0.29065, 0.03650). The experimental value for lattice constants a, b and c are 5.796, 5.817 and 8.205 Å, respectively.

As a first step, the lattice parameters were optimized to minimize the total energy with respect to unit cell of the ordered system, SZ-o, depicted in Fig. 1a. The calculated lattice constants were: $a = 5.776$ Å, $b = 5.788$ Å and $c = 8.154$ Å. Our theoretical lattice constant was only ~0.006% smaller than the experimental values and in good agreement with the experimental results. The optimized values of SZ-o cell parameters were calculated using the OPTIM [26] program. The band structures were obtained for 80 K points along the high-symmetry paths of the appropriate Brillouin zone.

Based on the experimental XANES results presented in this paper, three theoretical models (Fig. 1) were developed to simulate the disordered types and structural complex vacancies associated with them: (i) displacement of the network former, Zr (SZ-f); (ii) displacement of the network modifier, Sr (SZ-m); and (iii) simultaneous displacement in the network former–modifier, Zr/Sr (SZ-fm). Table 1 summarizes the aforementioned displacements.

To represent the complex vacancies of oxygen associated with the network former, Zr8 was shifted from its previous position in the unit cell of the network former (SZ-f model). This displacement causes asymmetries in the unit cell, in which Zr8 is now surrounded by five oxygens in a

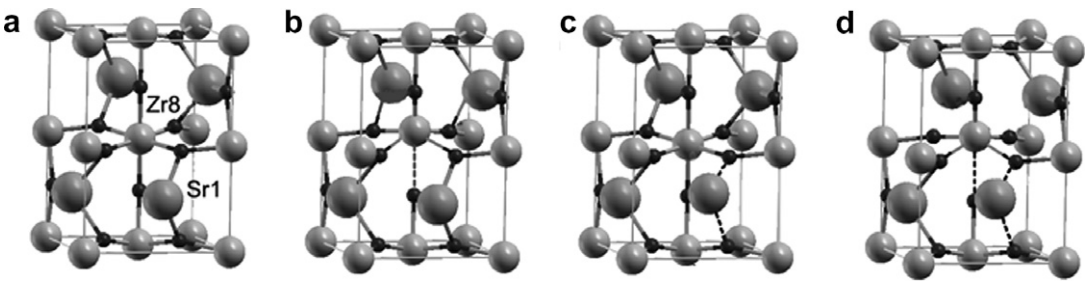

Fig. 1. (a) Ordered model of symmetric SZ-o; (b) asymmetric SZ-f model of network former displacement; (c) asymmetric SZ-m model of network modifier displacement and; (d) asymmetric model of network former and modifier displacement SZ-fm.

Table 1
SZ-f, SZ-m and SZ-fm vector displacements

SZ-f vector displacements (Å)	SZ-m vector displacements (Å)	SZ-fm vector displacements (Å)
Zr (000.1)	Sr (0.07100.071)	Zr (000.1); Sr (0.07100.071)
Zr (000.2)	Sr (0.14100.141)	Zr (000.2); Sr (0.14100.141)
Zr (000.3)	Sr (0.21200.212)	Zr (000.3); Sr (0.21200.212)
Zr (000.4)	Sr (0.28300.283)	Zr (000.4); Sr (0.28300.283)
Zr (000.5)	Sr (0.35000.350)	Zr (000.5); Sr (0.35000.350)

square-based pyramid configuration, while three other unit cells of Zr are surrounded by six oxygens, as in the case of SZ-o. Therefore, this asymmetric SZ model (SZ-f) represents the disorder in the network former material. This structure can be designated as $[ZrO_6]$–$[ZrO_5 \cdot V_O^Z]$, where $V_O^Z = V_O^X$, $V_O^{\cdot}$, $V_O^{\cdot\cdot}$, which gives rises to different complex clusters, depending on the displacement of the zirconium (Fig. 1b).

The network modifier disorder (SZ-m) was modeled by shifting the Sr1 from its previous position in the modifier unit cell. This displacement causes asymmetries in the unit cell, where Sr1 is now surrounded by 11 oxygens $[SrO_{11} \cdot V_O^X]$ while Sr2 is surrounded by 12 oxygens $[SrO_{12}]$, as in the case of SZ-o. Therefore, this asymmetric SZ model, SZ-m, represents the disorder in the network modifier material. This structure can be designated as $[SrO_{12}]$–$[SrO_{11} \cdot V_O^Z]$, depending on the displacement of the strontium (Fig. 1c).

Finally, the network former–modifier disorder (SZ-fm) was modeled at the same time by shifting both zirconium and strontium in the same way as described above. This displacement produces asymmetries in the unit cell, where Zr8 is now surrounded by five oxygens in a square-based pyramid configuration, while the other three Zr are surrounded by six oxygens, Sr1 is surrounded by 11 oxygens and Sr2 is surrounded by 12 oxygens. Therefore, in this asymmetric SZ model, SZ-fm represents the disorder in network former and modifier material. This structure can be designated as $[ZrO_6]$–$[ZrO_5 \cdot V_O^Z]$ and $[SrO_{12}]$–$[SrO_{11} \cdot V_O^Z]$ (see Fig. 1d). With these models, the effects of different structural disorders can be separately evaluated in terms of the electronic structure.

Ab initio calculations were made using the CRYSTAL98 [27] package within the framework of the density-functional theory (DFT), using the Lee–Yang–Parr gradient-corrected correlation functional combined with the Becke3 exchange functional, B3LYP [28,29], which Muscat et al. [30] demonstrated to be suitable for calculating the structural parameters and band structures of a wide variety of solids. The atomic centers were described by all electron basis sets 31(3d)G for Sr, 311d31G for Zr and 6-31G* for O [31]. To simulate the displacement of the Zr and Sr atoms we used the ATOMDISP option provided with the CRYSTAL program.

The DOS and energy band structures were calculated with the total 0.5 Å vector displacement of the network former and modifier in all the dislocated models.

These models can be useful for representing different degrees of order–disorder in the material, as well as structural defects resulting from network former and modifier displacements.

3. Results and discussion

Fig. 2 shows the evolution of the XRD patterns of SZ powders heat treated at 425, 450, 475, 500, 525, 550, 575, 600 and 1250 °C for 2 h under a flow of oxygen. XRD diffraction peaks are visible in powder annealed at 575, 600 and 1250 °C, indicating that, at these temperatures, the powders are structurally long-range ordered. The crystallization process of the structurally disordered SZ clearly starts at temperatures as low as 575 °C (see Fig. 2), and is completely ordered after annealing at 600 °C. Moreover, the XRD pattern of the SZ annealed at 600 and 1250 °C indicated that this material possesses a single phase, allowing for its complete indexation on the basis of an orthorhombic unit cell, according to ICDD card 42-423 (*Pbnm*).

Fig. 3 shows the Sr K-edge XANES spectra of the SZ powders as a function of annealing temperature. The main absorption peak of the K-edge of Sr can be assigned to 1s to 5p transitions [32].

The XANES spectrum of the powder annealed at 1250 °C corresponds to a well-crystallized SZ powder belonging to the *Pbmn* orthorhombic structure, as previously discussed. According to X-ray diffraction experiments, the powders showed long-range structural disorder below 550 °C. In this structure, approximately 12 oxygen atoms in a distorted structure coordinate Sr atoms, with Sr–O distances ranging from 2.57 to 2.91 Å. As can be seen in Fig. 3, at lower annealing temperatures, the feature situated around 16,130 eV and characteristic of the crystallized

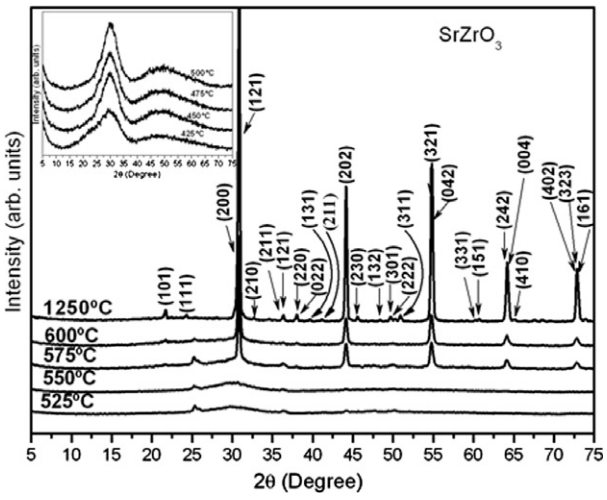

Fig. 2. XRD patterns of SZ powders for samples annealed at 525, 550, 575, 600 and 1250 °C for 2 h in a flow of oxygen. Inset shows SZ powders heat treated at 425, 450, 475 and 500 °C for 2 h in a flow of oxygen.

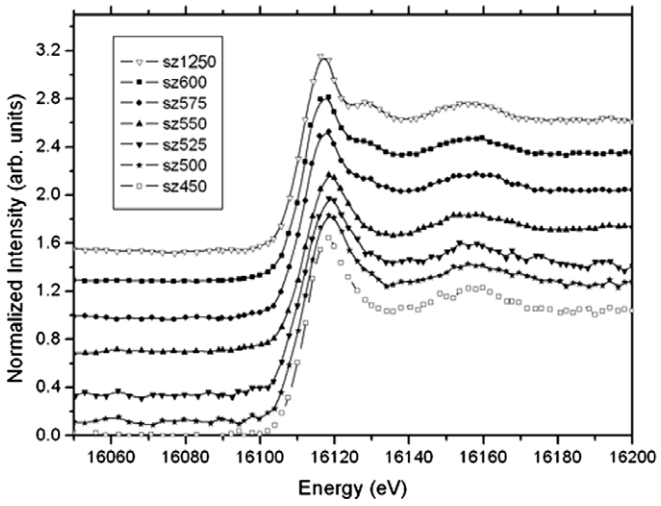

Fig. 3. K-edge XANES spectra of Sr of SZ powders annealed at 450, 500, 525, 550, 575, 600 and 1250 °C.

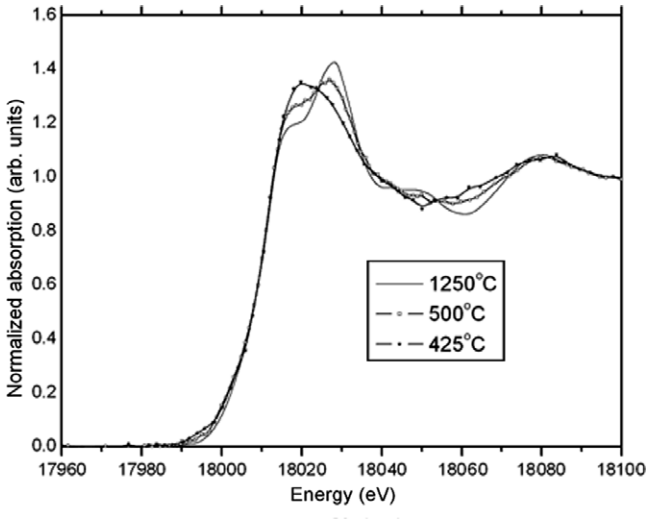

Fig. 4. Zr K-edge XANES spectra of SZ powders annealed at 425, 500 and 1250 °C.

samples disappears, and no significant difference is observed in the XANES spectra below 575 °C. Thus, Sr K-edge XANES shows that the local structure around Sr is quite similar when the annealing temperature rises to 550 °C and is characteristic of the presence of disorder in the Sr network modifier.

For the K-edge of Zr, the XANES spectrum of the powder annealed at 1250 °C (ordered sample) is quite similar to that found in the literature [33] (Fig. 4). In the orthorhombic structure, the first coordination shell around Zr atoms is composed of six oxygen atoms situated at 2.09 (2), 2.11 (2) and 2.14 Å (2). At lower annealing temperatures, these features become less evident and the XANES spectrum of the powder annealed at 425 °C is characteristic of zirconium in a locally disordered structure. At the annealing temperature of 500 °C, the absorption peak feature is not as defined as the totally ordered powder (1250 °C) but is quite similar. This result strongly indicates that, at the annealing temperature of 500 °C, the network former possesses a certain degree of short-range structural order.

In the powder annealed at 500 °C, the local structure measured by XANES indicates that the network former lattice has a certain degree of order, while the network modifier has a certain order only in samples annealed at temperatures above 575 °C. These results indicate that the network former became organized before the network modifier in the SZ lattice.

Fig. 5a shows the $k\chi(k)$ EXAFS spectra of SZ powders annealed at 500 and 1250 °C, while Fig. 5b shows the magnitude of its respective $k^3\chi(k)$ Fourier transform. Generally speaking, EXAFS spectra provide information about the coordination chemistry of the probe atom, such as average bond lengths and coordination numbers at the probe atom. XANES probes the density of unoccupied electronic states more directly. It complements EXAFS, providing

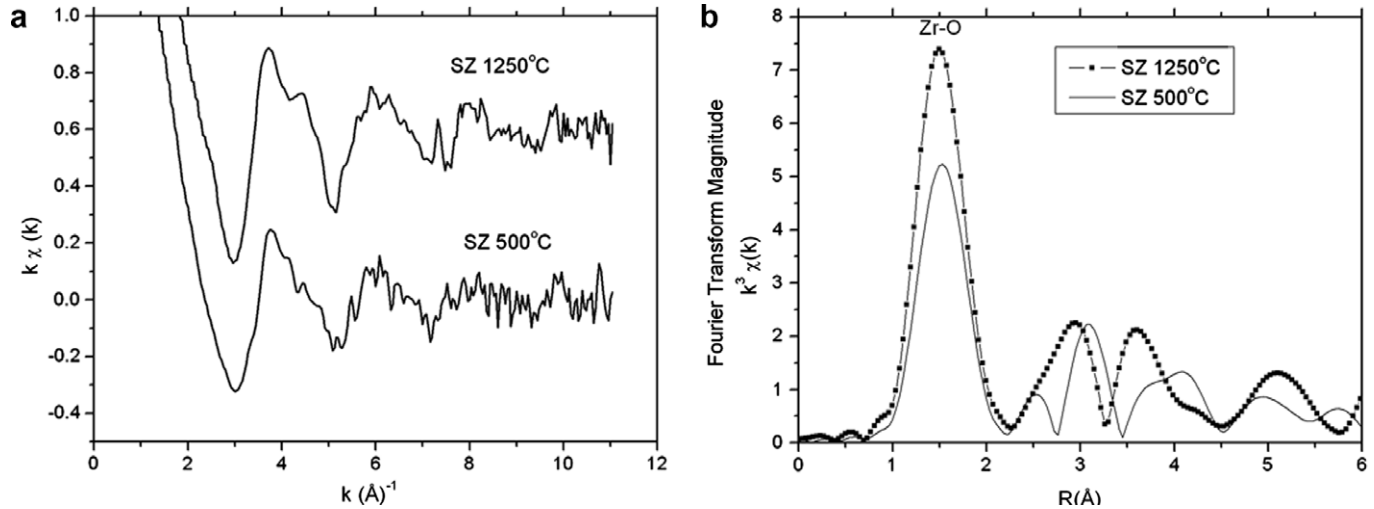

Fig. 5. (a) $k\chi(k)$ EXAFS spectra of SZ powders annealed at 500 and 1250 °C; (b) $k^3\chi(k)$ Fourier transform magnitude.

information on stereochemical features of the coordination polyhedron around the probe atom, including bonding configuration, ligand-field symmetry and valence state [32].

The first peak of the Fourier transform, located at around 1.5 Å in the EXAFS spectra of the SZ powders, corresponds to the first oxygen shell around Zr atoms and, as expected, the intensity of this first peak increased significantly with rising annealing temperature.

To quantitatively interpret this lower intensity of the SZ powder annealed at 500 °C, the contribution of the first coordination shell around zirconium atoms was extracted by a back-Fourier transform in the R distance space and then fitted using theoretical phase and amplitude functions obtained from the FEFF8 code. It is well known that the capability of EXAFS fitting of a multiple-distances model depends on the spatial resolution defined as $\Delta R = \pi/2k_{max}$, where k_{max} is the maximum value of the photoelectron momentum available in the recorded EXAFS spectrum. In our case, the k_{max} value is limited by the high level of noise at high K values. With $k_{max} = 11$ Å^{-1}, $\Delta R = 0.14$ Å. This means that Zr–O bond lengths that differ by less than 0.14 Å will not be resolved. According to XRD, all the Zr–O bond lengths in the first shell of SZ differ by less than 0.14 Å. On fitting EXAFS spectra we will consider only one shell with six neighbors. Despite this constraint, which precludes a correct evaluation of the Zr–O bond-length distribution and neighbor's number, we can carry out a fitting of the EXAFS spectra in order to analyze the behavior of the local disorder of the samples as a function of the annealing temperature. The local disorder can be analyzed in terms of the Debye–Waller factor (σ), which is defined as $\sigma^2 = \sigma_T^2 + \sigma_S^2$, where σ_S^2 is the static disorder term due to the fact that all the atoms in a particular shell cannot be at exactly the same distance from the central atom, and σ_T^2 is the thermal disorder because the atoms are not stationary but undergo a thermal vibration.

Table 2 presents the fitting results of the filtered EXAFS spectra of SZ powders annealed at 500 and 1250 °C. As can be noted, the decrease in the magnitude of the first peak of the Fourier transform can be interpreted as an increase in the value of the Debye–Waller factor of the sample annealed at 500 °C. Since both samples were measured at the same temperature, this increase is due to an increase in the static disorder (Zr–O bond lengths). Thus, although the Zr–O first coordination shell in the SZ ordered powder presents a relative degree of structural intrinsic disorder (three sets of Zr–O) distances, this degree of local disorder increases considerably in the disordered powder annealed at 500 °C.

Table 2
Structural results obtained from the fitting of the EXAFS spectra according to a shell model

Annealing temperature (°C)	N	σ^2 (Å^2)	R (Å)	ΔE_0 (eV)	QF
500	6	0.009 ± 0.002	2.14 ± 0.01	3 ± 1	1.40
1250	6	0.004 ± 0.002	2.10 ± 0.01	2 ± 1	1.45

N is the neighbor number, σ^2 is the Debye–Waller factor, R is the Zr–O mean bond length, ΔE_0 is the threshold energy shift and QF the quality factor defined according to Ref. [24]. The value of the neighbor number was fixed.

Due the tilted $[ZrO_6]$ cluster octahedra the ordered powder present an intrinsic $[ZrO_6]$ cluster distorted this presence cause the asymmetric in orthorhombic structure of SZ powder. This asymmetry makes it difficult to measure the $[ZrO_5]$ cluster experimentally, as in the EXAFS results of $SrTiO_3$, which has a simple cubic structure [15].

Nonetheless, in disordered SZ powders, oxygen displacement can be modulated by the presence of V_O^X, $V_O^{\cdot}$, $V_O^{\cdot\cdot}$ species, which are linked to the $[ZrO_5]$ clusters and give rise to complex clusters. In zirconates, these complex clusters can occur in three different charge states: the $[ZrO_5 \cdot V_O^X]$ complex state, which presents two paired electrons $\underline{\uparrow\downarrow}$ and is neutral relative to the lattice; the singly ionized $[ZrO_5 \cdot V_O^{\cdot}]$ complex state, which has one unpaired electron $\underline{\uparrow}$; and the $[ZrO_5 \cdot V_O^{\cdot\cdot}]$ complex state, which does not trap any electrons_ and is doubly positively charged with respect to the lattice. Another portion of electrons and holes may be trapped by intrinsic crystal defects in the network modifier $[SrO_{11} \cdot V_O^Z]$ complex cluster where $V_O^Z = V_O^X$, $V_O^{\cdot}$ or $V_O^{\cdot\cdot}$. These oxygen vacancies can be attributed to the Sr–O or Zr–O complex vacancy centers and were simulated theoretically by the SZ-f, SZ-m and SZ-fm models presented in Section 3.

Fig. 6a presents the experimental spectral dependence of the absorbance of the disordered SZ annealed at 450, 500 and 550 °C and ordered SZ powder annealed at 1250 °C. The ordered powder presents a well-defined absorption front while the structurally disordered powders typically exhibit a continuous smooth absorption increase as a function of the energy, suggesting the presence of localized states inside the band-gap. The optical gaps obtained by extrapolation of the linear curve regions according to the Wood and Tauc method [34] are 5.21 eV for the ordered sample and 4.50, 4.90 and 5.10 eV, respectively, for the disordered powders annealed at 450, 500 and 550 °C. These results indicate that the exponential optical absorption edge and the optical band-gap energy are controlled by the degree of structural disorder in the lattice. The decrease in the band-gap in structurally disordered powder can be attributed to defects and/or local bond distortion, which yield localized electronic levels in the band-gap of this material. Increased disorder is linked to deep defects inserted in the band-gap and increased order is associated with shallow defects, which disappear when total order is reached. However, the tail observed in the disordered samples indicates only the presence of defects and, hence, localized electronic levels in the forbidden band-gap, but cannot indicate the structural defects that may be linked to them.

For purposes of comparison with the experimental points, Fig. 6b presents the ab initio theoretical band-gap calculations for different displacements in the network modifier and network former. The calculations indicate the modifications that the structural changes cause in the

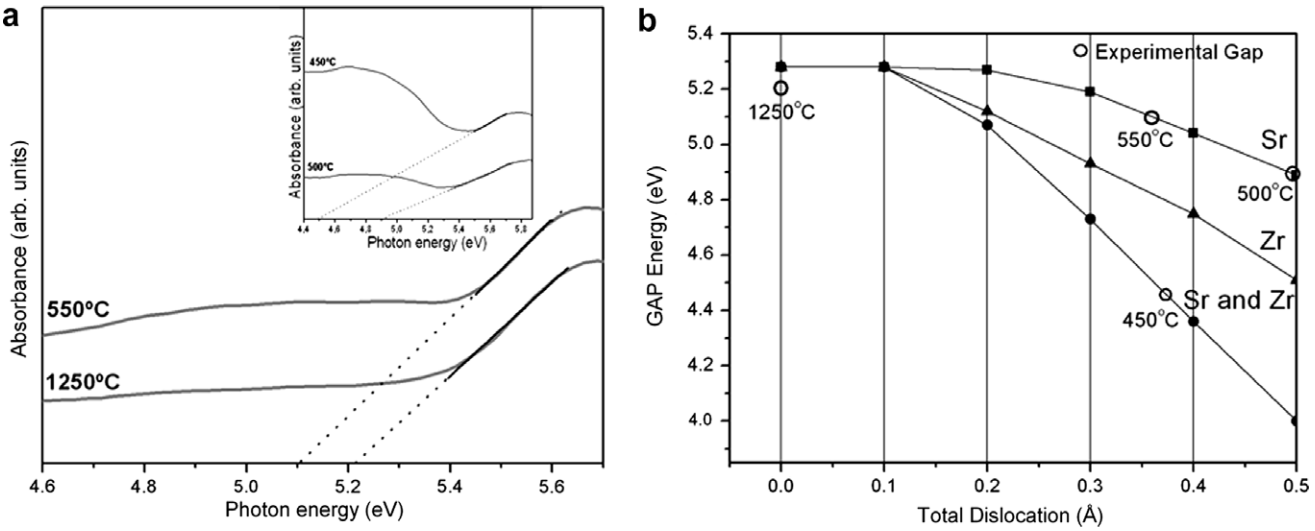

Fig. 6. (a) Spectral dependence of the absorbance of disordered SZ annealed at 450, 500 and 550 °C and ordered SZ powder annealed at 1250 °C for 2 h in a flow of oxygen. (b) Theoretical band-gap calculations for different displacements in the network modifier, network former and the network former–modifier.

gap state. It should be emphasized that the displacements which generated the theoretical models represented in this work were based on previous XANES results and do not reflect the exact reality of disordered powders. However, they provide an interesting scheme, shedding light on the effects of structural deformation on the electronic structure.

Displacement in the network former causes increased disorder in the lattice when compared with the network modifier. The greatest disorder occurs when both network former and modifier are displaced. This disorder is characterized by the reduction of the band-gap energy in the disordered models, leading to delocalized levels and an increase in the degeneracy of the orbital of the VB and the CB. Therefore, during the annealing process, there is a completely disordered structure represented by a disorder in the network former and modifier (powder annealed at 450 °C), an organization of the network former (powder annealed at 500 and 550 °C), and at least an organization of the network modifier (powder annealed at 1250 °C).

To analyze the differences in the electronic structure, it is convenient to make reference to quantities such as band structures, which can be compared to each other independently of the crystal space group. The calculated band structure also indicates the contributions of electronic states in the VB and CB. Fig. 7 shows the band structure of SZ-o, SZ-f, SZ-m and SZ-fm models with 0.5 Å of dislocation and the respective band-gaps derived from these models.

Fig. 7a depicts the calculated band structure of bulk SZ-o. The top of the VB is very close to the S point. The bottom of the CB is very close to the Γ point. The minimal indirect gap between S and Γ is 5.28 eV, which is close to the experimental value of 5.21 eV for crystalline powder annealed at 1250 °C deduced from the optical absorption edge.

The calculated band structure of bulk SZ-f is depicted in Fig. 7b. The top of the VB is close to the S point and bottom of the CB is close to Γ, as in case of SZ-o. The indirect minimal gap between S and Γ is 4.51 eV. This model represents only the electronic states derived from disorder in the former lattice and cannot be compared with an experimental powder because disorder solely in the network former is not possible. When the lattice former organizes at approximately 500 °C the modifier lattice is disordered, as discussed in the XANES results.

The calculated band structures of SZ-m and SZ-fm are reported, respectively, in Figs. 7c and d. The top of the VB is at Γ and bottom of the CB is at Γ in both cases. The direct minimal theoretical gap for the SZ-m model is 4.89 eV and was related to powder annealed at 500 °C (4.90 eV) and at 550 °C (5.10 eV) (see Fig. 6b). For the SZ-fm model, the calculated band-gap was 4.00 eV, which represents the major disorder of the lattice and disordered powder annealed at 450 °C (4.50 eV). These results indicate congruence between the experimental and theoretical data.

For the SZ-o (Fig. 7a), the VBs derive from the $2p_x$, $2p_y$, $2p_z$ orbitals of O atoms. They are separated by an indirect gap from the first CB, which derives from transition-metal zirconium ($4d_{xy}$, $4d_{xz}$, $4d_{yz}$) atomic orbitals, designated as "t_{2g}" by comparison with the [ZrO_6] regular cluster. Above these six bands are four Zr ($4d_{x^2-y^2}$ and $4d_{z^2}$) character bands designated as "e_g". For the displaced models (SZ-f, SZ-m and SZ-fm), although the VB is globally constituted of O ($2p_x$, $2p_y$, $2p_z$) character states, the top depends mainly on the axial oxygen located at the center of the structure, O11 and O12 for the SZ-f model, and planar oxygen O13, O15, O17 and O19 for the SZ-m and SZ-fm models. The CB is composed of the 4d states of zirconium in an apparently random splitting of bands (Figs. 7b–d).

The calculated total and atom-resolved DOS projected for the models SZ-o, SZ-f, SZ-m and SZ-fm are shown in Fig. 8, ranging from −2 eV below the top of the VB to 8 eV above and presenting the principal orbital that

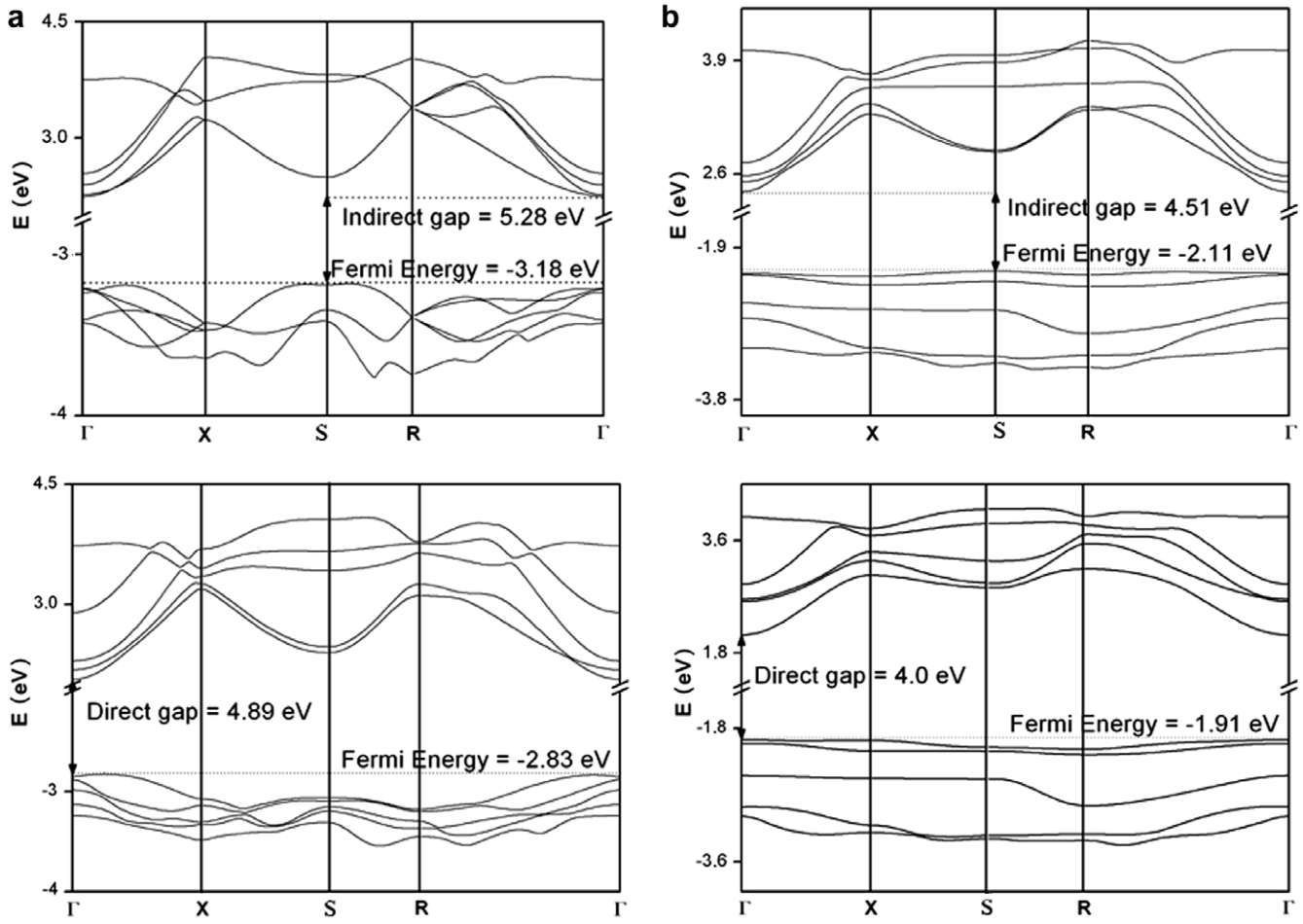

Fig. 7. Calculated energy band structures for: (a) SZ-o; (b) SZ-f; (c) SZ-m; (d) SZ-fm.

influences the gap state. The calculated atom-resolved projected DOS area of axial oxygen O11 and O12 and planar oxygen O13, O15, O17 and O19 for all the models was evaluated. This analysis was conducted only at the top of the VB, ranging from 0 eV to the Fermi energy, and was aimed at quantifying the contributions of the new 2p states of these oxygens created in the band-gap by the displacements of disordered models.

In the case of SZ-o, the upper VB is composed predominately of the O (2p) states, equivalently distributed in the axial oxygen O11 and O12 and planar oxygen O13, O15, O17 and O19 of the structure (Fig. 8a). In the case of SZ-f (Fig. 8b), although the VB is also composed of O (2p) states, the upper part, i.e. the new states, present a strong axial oxygen O11, O12 character (61%), which is the oxygen atom that loses the connection with Zr8 (Fig. 1). In the SZ-m case (Fig. 8c), the upper part of the VB is composed mainly of the planar 2p oxygen states O13, O15, O17 and O19 (78%). The SZ-fm structure has a strong axial oxygen contribution (63%) and is analogous to the SZ-f model, proving that the network former creates a split in degeneracy greater than that of the network modifier (Fig. 8d). The CB is clearly composed of the Zr (4d) states in the ordered and disordered structures. The Zr–O covalent bond creates a limited Zr (4d) contribution in the O (2p) region, as well as a weak O (2p) contribution to the Zr (4d) area.

The Sr (5s) states (not shown) are to be found at energies above −10 eV and are more dispersed in disordered models. These levels are weakly hybridized with oxygen levels in the SZ-f, SZ-m and SZ-fm model.

Fig. 9 illustrates PL spectra recorded at room temperature for the SZ powders heat treated at 425, 450, 475, 500, 525, 550, 575 and 600 °C in two different excitation wavelengths: 355 and 460 nm of an Nd:YAG laser.

The profile of the emission band is typical of a multiphonon and multilevel process, i.e. a system in which relaxation occurs by several paths, involving the participation of numerous states within the band-gap of the material. This behavior is related to the structural disorder of SZ and confirms the presence of additional electronic levels in the forbidden band-gap of the material.

The general aspect of the spectra is a broad band covering a large part of the visible spectra from ~370 to 800 nm. A set of emission bands is distinctly recorded under the two wavelengths, and the peak position of each band shifts upward as the excitation wavelength increases. This means that these two distinct energies (3.52 and 2.72 eV) are able

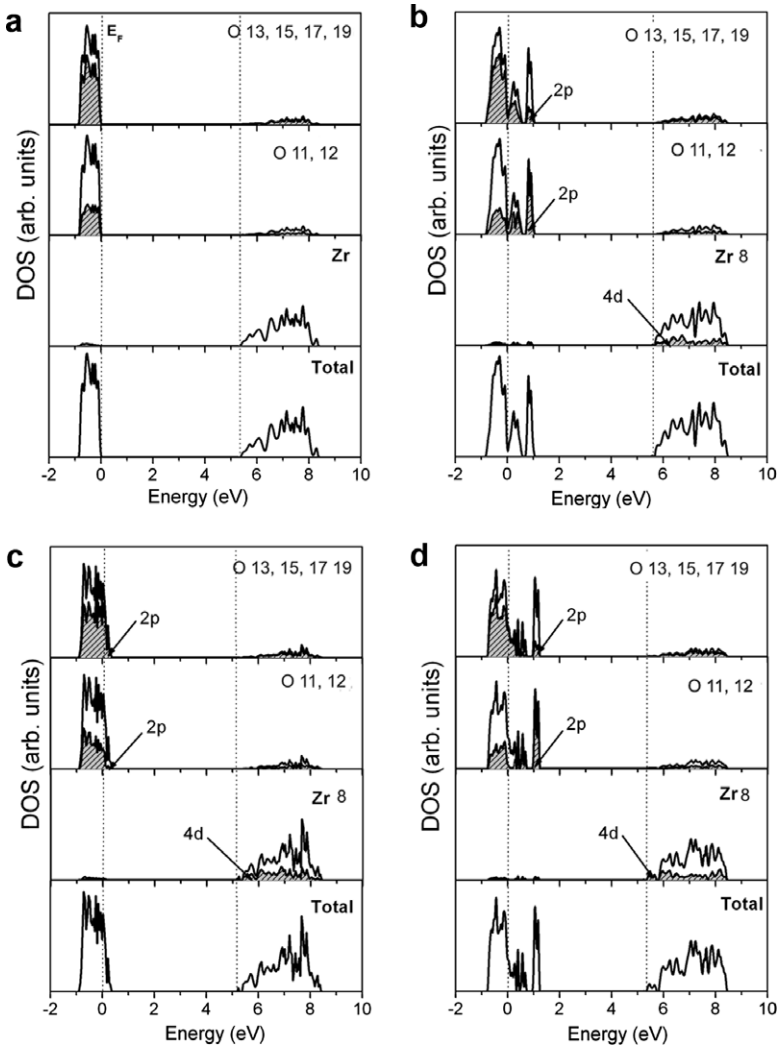

Fig. 8. Total and atom-projected density of states for: (a) SZ-o, (b) SZ-f, (c) SZ-m and SZ-fm models, where O12 and O13 are the axial oxygens and O13, O15, O17 and O19 are the planar oxygens.

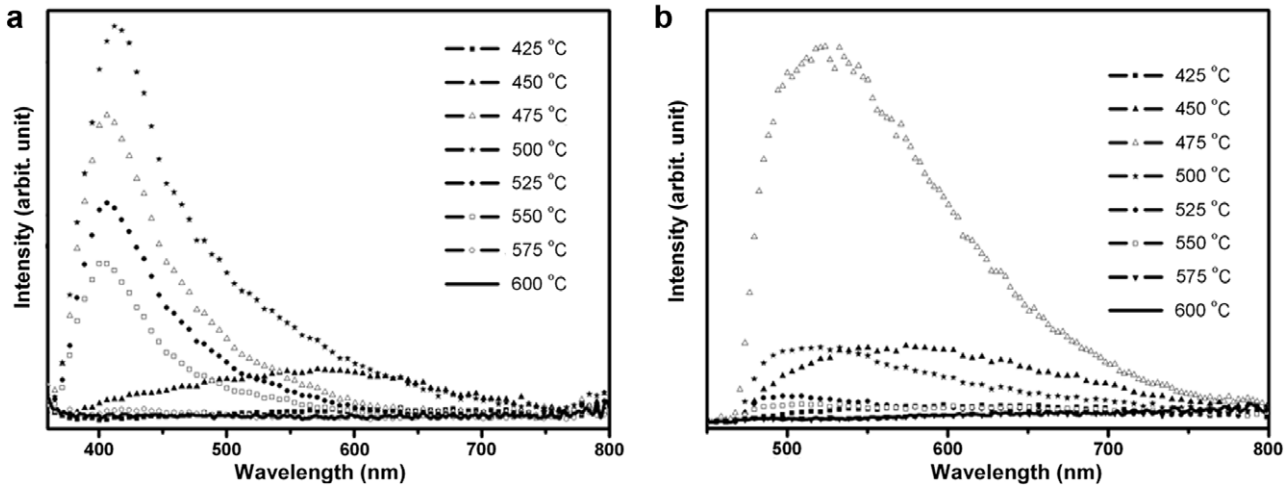

Fig. 9. (a) Room-temperature PL spectra of SZ powder samples annealed at 425, 450, 475, 500, 525, 550, 575 and 600 °C for 2 h in a flow of oxygen. (a) Excitation wavelength of an Nd:YAG laser at 355 nm. (b) Excitation wavelength of an Nd:YAG laser at 460 nm.

to excite different populations of electrons existing in the additional levels in the forbidden band-gap of disordered samples.

Quantum mechanical calculations of dislocated [ZrO_6] and/or [SrO_{12}] complex clusters indicate that localized states generated in the band-gap reduce the gap energies. When the structural order increases, the gap energy increases. These observations confirm the fact that PL is directly associated with the localized states existing in the band-gap and that the degree of order–disorder changes these localized states.

The strength of the electron–phonon interaction can be ascribed to the difference between the excitation and the emission maximum (Stokes shift). As can be seen, the Stokes shift decreases in the powder annealed at 475 °C for both excitation wavelengths. This indicates the dependence of the electron–phonon interaction on the excitation wavelength and on the degree of disorder in the lattice. This rearrangement of the lattice when the annealing temperature changes from 450 to 475 °C was clearly detected through PL experimental measurements and is a strong indication that this measurement is highly sensitive to structural changes.

The PL curves shown in Fig. 9 consist of six PL components, herein named the violet component (maximum below 438 nm), the blue component (maximum below 488 nm), the green component (maximum below 561 nm), the yellow component (maximum below 623 nm), the orange component (maximum below 625 nm) and the red component (maximum below 740 nm), alluding to the regions where the maxima of the components appear. In this sense, for a better understanding of the PL properties and their dependence on the structural order–disorder of the lattice, the PL curves were analyzed using a deconvolution PickFit [35]. Based on the Gaussian line-broadening mechanism for luminescence processes, the fine features in the PL spectra of samples annealed in the range 425–550 °C were deconvoluted, and features extracted from the deconvolution curves and the area under the curves of the respective transitions are listed in Tables 3 and 4.

Using the 355 nm excitation line and increasing the annealing temperature caused the structure of SZ powders to change to a more ordered structure, favoring violet–blue light emission (shorter wavelength) with higher energies. This violet–blue emission reached its maximum at 500 °C and its intensity was such that it was visible to the naked eye. At this annealing temperature, as previously discussed, the powder was long-range disordered and presented a certain short-range order, as indicated by our XANES measurements.

Table 3
Fitting parameters of the Gaussian peaks for PL obtained with an excitation wavelength of 355 nm

T (°C)	VC (%)[a]	BC (%)[a]	GC (%)[a]	YC (%)[a]	OC (%)[a]	RC (%)[a]
450	3	23	32	34	8	0
475	24	26	32	15	3	0
500	38	30	32	0	0	0
525	43	41	16	0	0	0
550	45	44	11	0	0	0

T, annealing temperature; components of PL: VC, violet; BC, blue; GC, green; YC, yellow; OC, orange; RC, red.
[a] Obtained by dividing the area of each decomposed PL curve by the total PL area.

Table 4
Fitting parameters of Gaussian peaks for PL obtained with an excitation wavelength of 460 nm

T (°C)	VC (%)[a]	BC (%)[a]	GC (%)[a]	YC (%)[a]	OC (%)[a]	RC (%)[a]
450	0	6	17	26	32	19
475	0	9	30	31	24	6
500	0	11	37	24	22	6
525	0	14	49	22	15	0
550	0	15	71	14	0	0

T, annealing temperature; components of PL: VC, violet; BC, blue; GC, green; YC, yellow; OC, orange; RC, red.
[a] Obtained by dividing the area of each decomposed PL curve by the total PL area.

Analogously, using an excitation wavelength of 450 nm caused a very intense green light emission to appear. The maximum of this emission was observed in the powder annealed at 475 °C. This powder was long- and short-range disordered. This greenish emission was greatly reduced in the powder annealed at 500 °C.

It should be pointed out that the visible emission band was not observed under an excitation of 2.72 eV in the sample annealed at 575 °C, but was observed with the 3.52 eV excitation line. This suggests that the corresponding excitation energy of 2.72 eV (460 nm) was unable to reach the lowest position of the localized levels in the band-gap of this sample.

The violet and blue emission can thus be attributed to shallow defects in the band-gap and to a more ordered structure, while the green, yellow and red emission is linked to defects deeply inserted in the band-gap and to a greater disorder in the lattice. In this sense, each color represents a different type of electronic transition and is linked to a specific structural arrangement. It can be inferred that an increased disorder in the lattice is associated with the presence of $[ZrO_5 \cdot V_O^{\cdot\cdot}]$ and $[ZrO_5 \cdot V_O^{\cdot}]$ complex clusters and that these complex defects are deeply inserted in the band-gap, leading to green–yellow–red PL emission. On the other hand, $[SrO_{11} \cdot V_O^{\cdot\cdot}]$ and $[SrO_{11} \cdot V_O^{\cdot}]$ complex clusters are linked to shallow defects in the band-gap and lead to a more energetic PL emission (violet–blue light). The deep defects linked to the network former disorder are associated with the 2p states of axial oxygens discussed in the presentation of DOS. The shallow defects can be ascribed to the 2p states of planar oxygens in the VB. Increasing the lattice order causes these complex vacancies and the PL emission to disappear.

The intensity of PL emission depends mainly on the interaction of these complex clusters and the excitation wavelength. Time-resolved spectroscopy is necessary to

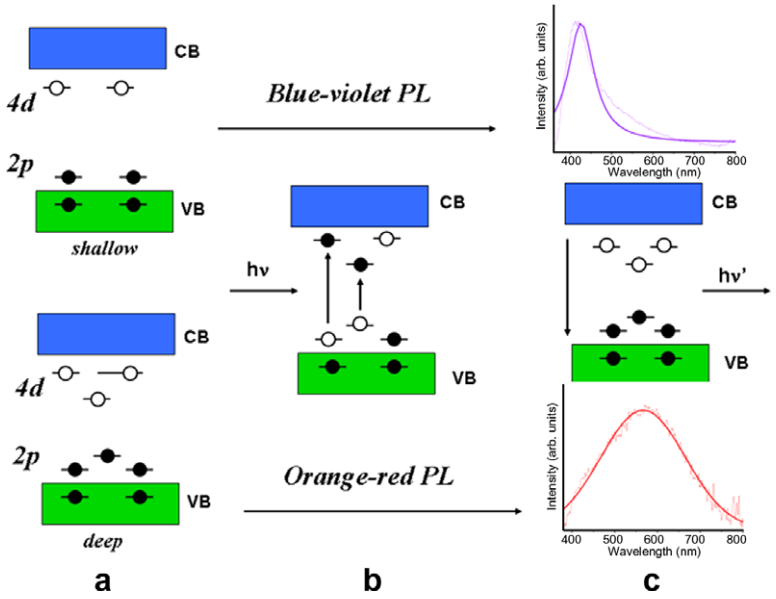

Fig. 10. Wide-band model: (a) before excitation, deep and shallow defects; (b) excitation—formation of self-trapped exciton; (c) after excitation—recombination of e^- and $h^{\bullet}$.

confirm this statement, which has already been investigated by several authors [36–39].

In our model, the wide-band model [22] presented in Fig. 10, the most important events occur before excitation, i.e. before the arrival of the photon. Deep and shallow oxygen complex clusters generate localized states in the band-gap and nonhomogeneous charge distribution in the cell, thereby allowing electrons to become trapped (Fig. 10). The localized levels are energetically distributed, so that various energies are able to excite the trapped electrons.

Before donor excitation, a hole in the acceptor state and an electron in the donor state are created according to the following equations, where the Kröger–Vink notation is used for complex clusters:

$$[ZrO_6]^X + [ZrO_5 \cdot V_O^X] \rightarrow [ZrO_6]' + [ZrO_5 \cdot V_O^{\bullet}], \quad (1)$$

$$[ZrO_6]^X + [ZrO_5.V_O^{\bullet}] \rightarrow [ZrO_6]' + [ZrO_5 \cdot V_O^{\bullet\bullet}], \quad (2)$$

$$[SrO_{12}]^X + [SrO_{11} \cdot V_O^X] \rightarrow [SrO_{12}]' + [SrO_{11} \cdot V_O^{\bullet}], \quad (3)$$

$$[SrO_{12}]^X + [SrO_{11} \cdot V_O^{\bullet}] \rightarrow [SrO_{12}]' + [SrO_{11} \cdot V_O^{\bullet\bullet}], \quad (4)$$

where $[ZrO_6]'$ or $[SrO_{12}]'$ are donors, $[ZrO_5 \cdot V_O^{\bullet}]$ or $[SrO_{11} \cdot V_O^{\bullet}]$ are donors/acceptors, and $[ZrO_5 \cdot V_O^{\bullet\bullet}]$ or $[SrO_{11} \cdot V_O^{\bullet\bullet}]$ are acceptors.

These equations suggest that the oxygen-vacancy-trapped electron in the VB is a necessary requirement for the transition of a VB hole in the CB. This is congruent with the experimental results of XANES measurements, which link the disorder in the lattice to inherent defects formed by oxygen deficiencies and the formation of $[ZrO_5 \cdot V_O^Z]$ and $[SrO_{11} \cdot V_O^Z]$ complex clusters. This means that most of the electrons around the oxygen vacancies are released and, therefore, such oxygen vacancy complex sites are relatively positive-charged. Moreover, oxygen vacancies tend to trap photogenerated electrons. The charge transfer that occurs as proposed in Eqs. (1)–(4) creates electron and hole polarons that can be designated as bipolarons.

In the complex, the $[ZrO_6]'$ or $[SrO_{12}]'$ clusters act as electron donors, while the vacancy complex $[ZrO_5 \cdot V_O^{\bullet}]$ and $[SrO_{11} \cdot V_O^{\bullet}]$ tends to trap electrons and/or holes and $[ZrO_5 \cdot V_O^{\bullet\bullet}]$ or $[SrO_{11} \cdot V_O^{\bullet\bullet}]$ act as electron traps. After excitation of the photon, the recombination and decay process follows the several valid hypotheses presented in the literature [36–39].

The present work shows that these complex clusters already existing in the ground state, proposed by the ab initio calculations, facilitate the emission process and lead to PL, i.e. the radiative recombination. Our ordered–disordered SZ powders thus intrinsically possess the necessary condition for creating PL at room temperature. The ordered powders do not allow for the creation of point defects and therefore do not present PL emission at room temperature.

4. Conclusions

Ultrafine $SrZrO_3$ powders were synthesized by a soft chemical process. The experimental results of XANES measurements of the disordered powders indicated that defects in the lattice are linked to defects formed by oxygen-deficient complex clusters. The results also indicate that the structural evolution from disorder to order occurs first in the network former and then in the network modifier. The results of first-principle calculations of the theoretical band-gap confirm the UV–vis results and indicate the changes in electronic states produced by structural displacements in network former and modifier. As the structural order increases, so does the gap energy.

The two excitation lines used for the PL measurements enabled us to understand the various populations of levels that already exist in the disordered powder, which was also confirmed by the ab initio periodic calculation.

The increased disorder in the lattice was associated with the presence of $[ZrO_5 \cdot V_O^{\cdot}]$ and $[ZrO_5 \cdot V_O^{\cdot\cdot}]$ complex clusters (disorder in the network former) and attributed to defects deeply inserted in the band-gap, leading to green–yellow–red PL emission. In this sense, the $[SrO_{11} \cdot V_O^{\cdot}]$ and $[SrO_{11} \cdot V_O^{\cdot\cdot}]$ complex clusters (disorder in the network modifier) were associated with shallow defects in the band-gap and with the violet–blue light. As the order in the lattice increased, these complex vacancies gradually disappeared, as did the PL emission.

Acknowledgements

The authors would like to thank the Brazilian research financing institutions FAPESP/CEPID, CNPq/PRONEX and CAPES for their funding of this work. This research was partially conducted at the LNLS (National Laboratory of Synchrotron Light, Brazil).

References

[1] Slonimskaya EA, Belyakov AV. Glass Ceram 2001;58:54.
[2] Iwahara H, Yajima T, Hibino T, Ushida H. J Eletrochem Soc 1993;140:1687.
[3] Kurita N, Fukatsu N, Ohashi T. J Jpn Inst Met 1994;58:782.
[4] Yajima T, Koide K, Takai H, Fukatsu N, Iwahara H. Solid State Ionics 1995;79:333.
[5] Higuchi T, Tsukamoto T, Matsumoto H, Shimura T, Yashiro K, Kawada T, Mizusaki J, Shin S, Hattori T. Solid State Ionics 2007;176:2435.
[6] Roth RS. J Res Natl Bur Stand 1957;58:75.
[7] Swanson HE, Cook MI, Isaacs T, Evans EH. Natl Bur Stand Circ 1960;539:51.
[8] de Ligny D, Richet P. Phys Rev B 1996;53:3013.
[9] Kennedy BJ, Howard CJ, Chakoumakos BC. Phys Rev B 1999;59:4023.
[10] Matsuda T, Yamakama S, Kurosaki K, Kobayashi S. J Alloys Compd 2003;351:43.
[11] Canham LT. Appl Phys Lett 1990;57:1046.
[12] Pizani PS, Basso HC, Lanciotti F, Boschi TM, Pontes FM, Longo E, Leite ER. Appl Phys Lett 2002;81:253.
[13] Orhan E, Varela JA, Zenatti A, Gurgel MF, Pontes FM, Leite ER, Longo E. Phys Rev B 2005;71:085113.
[14] Longo E, Orhan E, Pontes FM, Pinheiro CD, Leite ER, Varela JA, Pizani PS, Boschi TM. Phys Rev B 2004;69:125115.
[15] Pontes FM, Longo E, Leite ER, Varela JA, Lee EJH, Pizani PS, Campos CEM, Lanciotti Jr F, Mastellaro V, Pinheiro CD. Mater Chem Phys 2002;77:598.
[16] Pinheiro CD, Longo E, Leite ER, Pontes FM, Magnani R, Varela JA, Pizanni PS, Boschi TM, Lanciotti F. Appl Phys A 2003;77:81.
[17] Schroder DK. Semiconductor material and device characterization. New York: John Wiley; 1990.
[18] Zhang WF, Tang JW, Ye JH. Chem Phys Lett 2006;418:174.
[19] Chen F, Liu HW, Wang KF, Yu H, Dong S, Chen XY, Jiang XP, Ren ZF, Liu JM. J Phys.: Condens Matter 2005;17:L467.
[20] Zhang MS, Yu J, Chu JH, Chen Q, Chen WC. J Mater Process Techn 2003;137:78.
[21] Zhang A, Lu M, Wang S, Zhou G, Wang S, Zhou Y. J Alloys Compd 2007;433:L7.
[22] Longo VM, Cavalcante LS, de Figueiredo AT, Santos LPS, Longo E, Varela JA, Sambrano JR, Paskocimas CA, De Vicente FS, Hernades AC. Appl Phys Lett 2007;90:091906.
[23] Kakihana M, Yoshimura M. Bull Chem Soc Jpn 1990;72:1427.
[24] Michalowicz A. J Phys IV 1997;7:C2–C235.
[25] Report on the International Workshops on Standards and Criteria in XAFS. In: Hasnain SS, editor. X-ray absorption fine structure: proceedings of the VI international conference on X-ray absorption fine structures. New York: Ellis Horwood; 1991. p. 752.
[26] Cabal VL. OPTIM user's manual. Oviedo (Spain): Depatamento de Química y Física Analitica, University of Oviedo; 1998.
[27] Saunders VR, Dovesi R, Roetti C, Causa M, Harrison NM, Zicovich-Wilson CM. CRYSTAL98 user's manual. Torino (Italy): University of Torino; 1998.
[28] Lee C, Yang W, Parr RG. Phys Rev B 1988;37:785.
[29] Becke AD. J Chem Phys 1993;98:5648.
[30] Muscat J, Wander A, Harrison NM. Chem Phys Lett 2001;342:397.
[31] http://www.tcm.phy.cam.ac.uk/~mdt26/crystal.html.
[32] Wang CM, Slade Cargill G, Chan Helen M, Harmer Martin P. J Am Ceram Soc 2002;85:2492.
[33] Kamishima O, Ohta K, Chiba Y, Hattori T. J Phys: Condens Matter 2001;13:2455.
[34] Wood DL, Tauc J. Phys Rev B 1972;5:3144.
[35] Ding T, Zheng WT, Tian HW, Zang JF, Zhao ZD, Yu SS, Li XT, Meng FL, Wang YM, Kong XG. Solid State Commun 2004;232:815.
[36] Leonelli R, Brebner JL. Solid State Commun 1985;54:505.
[37] Leonelli R, Brebner JL. Phys Rev B 1986;33:8649.
[38] Eglitis RI, Kotomim EA, Bostel G. Eur Phys J B 2002;27:483.
[39] Eglitis RI, Kotomim EA, Bostel G. J Phys: Condens Matter 2002;14:3735.